TRENDS IN SCIENCES 2026; 23(4): 11966
https://doi.org/10.48048/tis.2026.11966 RESEARCH ARTICLE

Solasodine-Loaded MCM-41 Mesoporous Silica for Targeted Anticancer Delivery: Insights from Preparation, Characterization, and Adsorption Studies

Rohmatun Nafi'ah[1,2], Sri Juari Santosa[1,*], Sutarno Sutarno[1] and Eti Nurwening Sholikhah[3]

[1]*Department of Chemistry, Faculty of Mathematics and Natural Sciences, Universitas Gadjah Mada, Yogyakarta 55281, Indonesia*
[2]*Department of Pharmacy, Institut Teknologi Kesehatan Cendekia Utama Kudus, Jawa Tengah 59381, Indonesia*
[3]*Department of Pharmacology and Therapy, Faculty of Medicine, Public Health, and Nursing, Universitas Gadjah Mada, Yogyakarta 55281, Indonesia*

([*]Corresponding author's e-mail: sjuari@ugm.ac.id)

Received: 19 September 2025, Revised: 21 October 2025, Accepted: 28 October 2025, Published: 30 December 2025

Abstract

Mesoporous silica Mobil Composition of Matter No. 41 (MCM-41) has gained considerable attention as a carrier matrix because of its large surface area, adjustable pore size, and biocompatibility. This study aimed to prepare and thoroughly characterize MCM-41 using a sonochemical approach and to evaluate its potential for adsorbing solasodine, a steroidal alkaloid with anticancer properties. MCM-41 was prepared under different sonication times (30 - 150 min) and characterized using Fourier Transform Infrared Spectroscopy (FTIR, X-ray Diffraction (XRD), Transmission Electron Microscopy (TEM), Scanning Electron Microscopy coupled with Energy Dispersive X-ray (SEM-EDX), and Brunauer-Emmett-Teller (BET) techniques. XRD results confirmed the formation of a well-defined hexagonal mesostructure, with crystallinity increasing with increasing sonication time. Loading solasodine onto MCM-41 reduced diffraction intensity but preserved the structural framework. BET analysis revealed decreases in surface area (from 1129.39 to 849.31 m^2/g), pore volume (from 0.87 to 0.59 cc/g), and pore diameter (from 3.41 to 2.17 nm), indicating successful solasodine incorporation. Adsorption of solasodine was optimum at pH 4, followed well a kinetic model of second order reaching equilibrium and an isotherm model of Langmuir with an adsorption capacity of 1.69×10^{-2} mmol/g, indicating strong carrier affinity and monolayer adsorption.

Keywords: MCM-41, Solasodine, Adsorption, Sonochemical preparation, Mesoporous silica

Introduction

The development of drug delivery systems (DDS) has attracted attention in biomedical research over the last 2 decades [1,2]. DDS can effectively improve drug bioavailability [3,4], stability [5,6], extend drug release [7,8], and minimize toxic consequences [9]. In cancer therapy, the response to chemotherapeutic agents is often limited by their toxicity to healthy tissues [10]. Therefore, effective treatment relies on innovative DDS strategies to enhance efficacy [11,12] and reduce side effects [13].

One of the most promising materials for DDS is Mobil Composition of Matter No. 41 (MCM-41), a mesoporous silica with a highly ordered pore structure [14]. MCM-41 possesses a large surface area, uniform pore diameter, large pore volume, and good biocompatibility [15-25]. These combined characteristics make MCM-41 an excellent carrier matrix for DDS.

Meanwhile, solasodine is a natural steroidal alkaloid derived from Solanum species that exhibits notable anticancer potential through apoptosis induction

and inhibition of tumor cell proliferation, as evident from different *in vitro* and *in vivo* studies [26,27]. Despite such activities, solasodine exhibits low aqueous solubility and physicochemical instability, limiting its therapeutic use [28]. Given these physicochemical advantages, MCM-41 holds significant potential as a DDS for solasodine. Its use may improve solasodine's bioavailability, stability, and therapeutic performance.

Although MCM-41 has been studied for other compounds such as curcumin, paclitaxel, and doxorubicin [29-33], its application for solasodine adsorbent has not, to the best of our knowledge, been explored. Understanding the interaction between MCM-41 and solasodine is essential for identifying the factors that control loading efficiency and for optimizing delivery.

In this study, MCM-41 was prepared using a sonochemical method, thoroughly characterized, and subsequently applied as an adsorbent for solasodine. Key adsorption parameters, including solution pH, contact time, and initial solasodine concentration, were optimized. The resulting data were used to evaluate adsorption kinetics and isotherms. Furthermore, efforts were made to elucidate the underlying adsorption mechanism. The findings of this study are expected to serve as a foundation for further development of MCM-41-based solasodine delivery systems.

As opposed to previous research that has focused on encapsulation of other well-documented anticancer compounds such as curcumin, doxorubicin, and paclitaxel within mesoporous silica carriers, this study takes into account solasodine, which is a steroidal alkaloid with inherent amphiphilic and physicochemical characteristics that influence its adsorption and interaction with silica interfaces. Adsorption and carrier properties of solasodine in MCM-41 are, to our knowledge, not previously reported. Moreover, the use of a sonochemical process enables energy-conserving, quick preparation to increase structural ordering and surface reactivity, providing a novel approach to the preparation of MCM-41 nanocarriers for natural alkaloids.

Materials and methods

Materials

Preparation of MCM-41 involves the use of cetyltrimethylammonium bromide (CTAB; Merck) as a directing agent for structure, sodium silicate solution (Na_2SiO_3; 22% - 25% SiO_2, 8% Na_2O, 65% H_2O, all on %w/w basis; Merck) as silica precursor, ethyl acetate (EtAc; Merck) as a co-solvent and distilled water as the reaction medium. During the Preparation process, the molar ratio was 1.0 Si, 0.33 CTAB, 1.86 EtAc, 450 H_2O. Solasodine (**Figure 1**) with chemical formula $C_{27}H_{43}NO_2$ and molecular mass 413.646 g/mol was obtained from a commercial supplier.

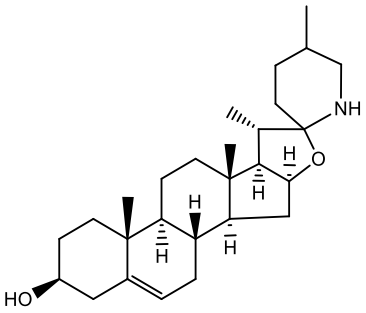

Figure 1 Chemical structure of solasodine [35].

Methods

Preparation of MCM-41

First, 100 mL of distilled water was used to dissolve 1.62 g of CTAB while stirring for 30 min. Subsequently, 3.88 g of Na_2SiO_3 was added to the solution and stirred for 1 h until a white slurry was obtained. Thereafter, 2.24 g of EtAc was introduced into the mixture, followed by rapid stirring for an additional hour.

The final mixture was sonicated using a Bransonic 220 ultrasonic reactor (48 kHz, 100 W) for different periods (30, 60, 90, 120 and 150 min) and left to stand

overnight. The precipitation was filtered, washed repeatedly with distilled water, and the pH of the filtrate (washing water) was measured until neutrality (pH ≈ 7) was achieved, and dried in an oven (Fisher Scientific 655 K) at 110 °C for 6 h. The CTAB surfactant was then removed by calcination in a furnace (FB 1310 M-33) at 550 °C for 6 h to obtain the mesoporous MCM-41 structure.

Characterisation of MCM-41 and solasodine

A variety of characterization techniques were used for the characterization of the prepared materials of MCM-41, including FTIR spectroscopy for functional group analysis, XRD for crystallographic structure determination, TEM for morphological and structural assessment, and SEM-EDX for surface morphology and elemental composition analysis. In addition, nitrogen adsorption-desorption isotherms were used to measure surface area, pore size distribution, and porosity. In the case of solasodine, it was studied using FTIR spectroscopy to identify functional groups.

Commercial MCM-41 (Sigma-Aldrich) was used as a control sample to serve as a reference for the evaluation of the sonochemical preparation effect on adsorption and structural characteristics. Comparative XRD, FTIR, SEM, and TEM studies were conducted between commercial and obtained MCM-41 to verify the integrity and maintenance of mesostructure.

Adsorption study of solasodine on MCM-41

Batch adsorption experiments were performed in varying 3 key parameters, namely solution pH, contact time, and initial concentration of solasodine to investigate the adsorption behavior of solasodine on MCM-41. All adsorption experiments were carried out at room temperature (25 ± 2 °C) to simulate physiological conditions and ensure reproducibility.

The effect of pH

The effect of pH on solasodine adsorption was studied in the pH range 1 - 8. The stock solution of 1,000 µg/mL of solasodine was obtained by dissolving 10 mg of solasodine in 10 mL of methanol. 10 mL of stock solution in methanol was diluted with distilled water to 100 mL to get a working solution (100 µg/mL). The final solvent composition obtained was 10 %(v/v) methanol.

For every experiment, 0.1 g of MCM-41 was mixed with 20 mL of the working solution. The pH of the solution was adjusted using standardized 0.1 M hydrochloric acid (HCl) and 0.1 M sodium hydroxide (NaOH) solutions. The suspensions were shaken at room temperature (25 ± 2 °C) for 24 h. The residual solasodine was analyzed using UV-Vis spectrophotometry after filtration. Each maximum wavelength was checked before analysis. Non-adsorptive solasodine losses were checked in control experiments without MCM-41.

Determination of the point of 0 charge (pH_{PZC})

The pH_{PZC} of MCM-41 was determined by the pH drift method within the pH range 1 - 8. Concisely, 20 mL of 0.01 M NaCl solution having an initial pH between 1 and 8 adjusted using 0.1 M HCl or NaOH was added to 0.1 g of MCM-41 and stirred at 25 ± 2 °C for 24 h. After equilibration, the pH_final was measured, and the pH_{PZC} was taken as the point where ΔpH = 0, and ΔpH = pHf - pHi was plotted versus pHi.

The effect of contact time and the determination of adsorption kinetics

The effect of contact time on the adsorption of solasodine was evaluated by suspending 0.5 g of MCM-41 in 20 mL of solasodine solution (50 µg/mL) in methanol–water (10:90 v/v) at the optimum pH of 4. The suspensions were agitated at room temperature (25 ± 2 °C) for varied time intervals: 15, 30, 45, 60, 75, 90, 120, and 150 min. At every time point, the suspensions were filtered, and the remaining solasodine concentrations were measured by UV-Vis spectrophotometry. The control samples without MCM-41 were also prepared and subjected to the same treatment to correct for solasodine loss not due to adsorption.

Based on the data of the effect of contact time, the kinetics of adsorption of solasodine on MCM-41 were then examined. The kinetic models were fitted utilizing 3 different models: The pseudo-first-order (Eq. (1)) model from Lagergren [36], the pseudo-second-order (Eq. (2)) model from Ho and McKay [37], and the second-order reaching equilibrium model (Eq. (3)) from Santosa [38].

$$\ln(q_e - q_t) = -k_{1p}t + \ln q_e \quad (1)$$

$$\frac{t}{q_t} = \frac{1}{k2_p q2_e} + \frac{1}{q_e} t \quad (2)$$

$$\frac{1}{C_e}\left[\ln\left\{\frac{C_t(C_o - C_e)}{C_o(C_t - C_e)}\right\}\right] = k2t \quad (3)$$

The pseudo-first-order, pseudo-second-order, and second-order reaching equilibrium kinetic model rate constants are k_{1p}, k_{2p}, and k_2, respectively. C_0 and C_e are the initial concentration and the concentration of solasodine in solution (mmol/L), while qt and qe are the amount of solasodine adsorbed at adsorption time t and at equilibrium per unit mass of the adsorbent (mmol/g), respectively.

The kinetic parameters were found from the linear regression fit (R^2 values) of the individual kinetic model by making their respective linear forms: $\ln(q_e\text{-}q_t)$ against t for pseudo-first-order, t/q_t against t for pseudo–second–order, and $\frac{1}{C_e}\left[\ln\left\{\frac{C_t(C_o - C_e)}{C_o(C_t - C_e)}\right\}\right]$ against t for the Santosa second–order reaching equilibrium model.

The effect of concentration of solasidine and the determination of the adsorption isotherm

MCM-41, as much as 0.5 g, was dispersed in 20 mL of methanolic solution (10:90 v/v) of solasodine with different concentrations (10, 15, 50, 100, 150, 200 and 250 µg/mL) at the optimum pH of 4 and an equilibrium contact time of 90 min. The suspensions were shaken at room temperature (25 ± 2 °C) for 24 h. After equilibration, suspensions were filtered and their remaining concentration of solasodine was analyzed using UV-Vis spectrophotometry. In addition, control samples without MCM-41 were prepared at all concentrations of solasodine to account for any potential loss of solasodine due to factors unrelated to adsorption.

To gain a better understanding of the interaction between solasodine and the MCM-41 adsorbent. The adsorption isotherm models employed in this investigation were the Langmuir, the Freundlich, and the Temkin isotherm models as given by Eqs. (4) - (6), respectively.

$$\frac{C_e}{q_e} = \frac{1}{q_m K_L} + \frac{C_e}{q_m} \quad (4)$$

$$\log q_e = log\ K_F + \frac{1}{n}\log C_e \quad (5)$$

$$\log q_e = \left(\frac{R.T}{bT}\right)\ln K_T + \left(\frac{R.T}{bT}\right)\ln C_e \quad (6)$$

C_e and q_e are the concentration of solasodine in solution (mmol/L) and the amount of solasodine adsorbed per unit mass of MCM-41 (mmol/g) at equilibrium, respectively. q_m and K_L are the Langmuir adsorption capacity (mmol/g) and adsorption intensity (L/mmol), respectively. K_F is the Freundlich adsorption constant (mmol/g), $1/n$ is the heterogeneity factor, bT (J/mol) is the Temkin adsorption energy, which is correlated with the adsorption heat, and K_T (L/mmol) is the Temkin isotherm equilibrium constant.

All adsorption experiments were performed in triplicate for reproducibility purposes. Experimental data were plotted as mean ± standard deviation (SD). Parameters of kinetic and isotherm models were obtained through nonlinear regression fitting using OriginPro 2025 software, and the correlation coefficient (R^2) was used to estimate the goodness of fit.

Results and discussion

XRD confirmation in MCM-41 Preparation and changes after solasodine adsorption

XRD was employed to characterize the crystalline nature of the prepared MCM-41 materials prepared using various sonication times (30, 60, 90, 120 and 150 min), providing a hint about the mesostructural ordering. **Figure 2(A)** shows 3 well-resolved diffraction peaks at low 2θ angles for all prepared MCM-41 at various sonication times, corresponding to the [100], [110], and [200] reflections characteristic of the highly ordered hexagonal mesoporous structure. The (100) peak ranged between 2θ = 2.21° - 2.32°. The calculated lattice constants (4.52 - 4.61 nm) and interplanar spacings (d_{100} = 3.91 - 3.99 nm) are consistent with reported values for MCM-41, which confirms the hexagonal mesoporous structure formation. The small discrepancies arise from the impact of sonication time on silica condensation and micelle ordering, and this slightly influences structural ordering. Interestingly, all the peaks that were observed were in good agreement with standard MCM-41 reference patterns (JCPDS No. 49-1712), reflecting the successful Preparation of hexagonally ordered mesoporous silica.

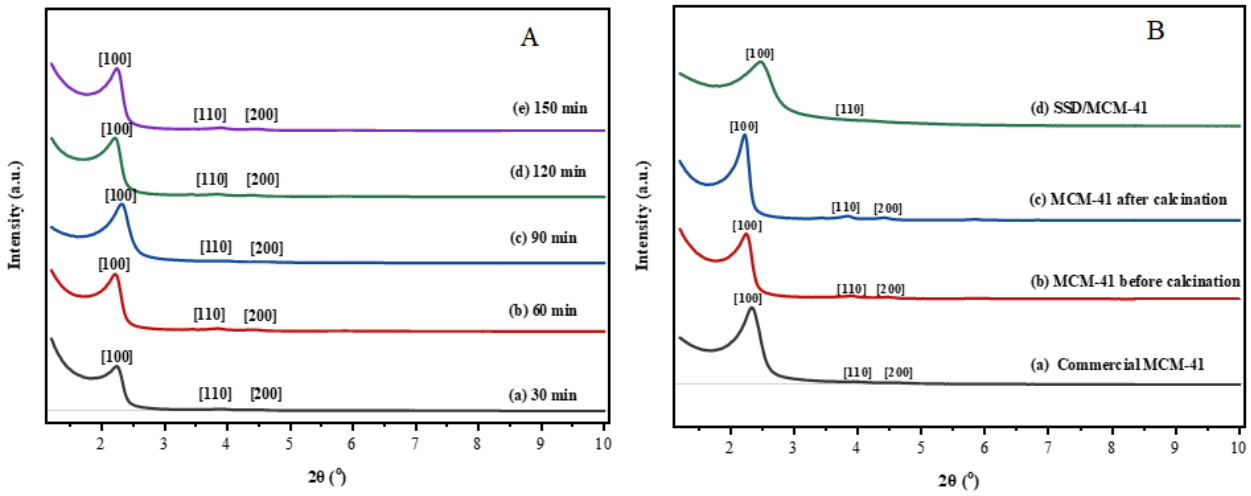

Figure 2 (A) X-ray diffractogram of prepared MCM-41 with a variation of sonication time; (B) X-ray diffractograms of commercial MCM-41, MCM-41 before calcination, MCM-41 after calcination, and MCM-41 after being used to adsorb solasodine (SSD/MCM-41).

As evident from **Table 1**, the relative crystallinity of all the prepared MCM-41 samples was high (> 99.5%), ensuring that changing sonication time had not disrupted hexagonal order. Pore diameter (D_{XRD}) estimated by subtracting a 1 nm wall thickness from a_o ranged between 3.52 and 3.60 nm, confirming mesoporous character. As is evident, the 150-min sample recorded the highest peak intensity (26,932 counts) and crystallinity (99.7%), ensuring that increased sonication enhances mesostructural ordering.

Table 1 Structural data of prepared MCM-41 with a variation of sonication time.

Sonication time (min)	2θ (°)	Intensity (count)	Relative Crystallinity[a] (%)	d_{100} (nm)	a_o[b] (nm)	D_{XRD}[c] (nm)
30	2.24	19,799	99.5	3.94	4.55	3.55
60	2.22	24,869	99.6	3.99	4.60	3.60
90	2.32	25,214	99.6	3.91	4.52	3.52
120	2.21	25,572	99.6	3.99	4.61	3.61
150	2.24	26,932	99.7	3.94	4.55	3.55

Notes: [a] means the value for the best-defined intensity of the sample; [b] plane lattice parameter [100] using the formula $a_o = 2d/\sqrt{3}$; and [c] the approximate value of pore diameter, $D_{XRD} = a_o$ (nm)-1(nm), assuming that the wall thickness of pore was relatively stable (1 nm).

The sonochemical process in this research was modified and optimized from earlier procedures [39], with alterations in precursor proportion, sonication energy, and time. These modifications increased the crystallinity and homogeneity of MCM-41. Calcination of the prepared MCM-41 at 150 min sonication time results in higher peak intensity and 2θ (**Figure 2(B)**). This modification is linked to the decreased lattice parameters by extracting cationic surfactant CTAB, which significantly promotes structural shrinkage and improves crystallinity. Upon CTAB extraction, the mesoporous structure is more ordered because the extraction of surfactant micelles produces well-defined channels. The condensation of silica units that occurs on calcination stabilizes the framework and yields a more

crystalline hexagonal mesostructure with unit cell dimensions slightly reduced.

Figure 2(B) also shows commercial MCM-41 used as the control, which is characterized by a strong diffraction peak at 2θ ≈ 2.33°. MCM-41, after being used to adsorb solasodine (SSD/MCM-41), shows pore diameter reduction from 3.59 to 3.14 nm, and the intensity of the [100] diffraction peak is also reduced (**Table 2**). This indicates reduced mesoporosity due to solasodine adsorption, which indirectly demonstrates the successful loading of solasodine in the mesoporous framework.

XRD patterns confirmed the hexagonal mesostructure of MCM-41, which was preserved after loading with solasodine. Maintenance of regular mesopores is crucial to ensure even distribution of drugs in the carrier and improve controlled diffusion during drug release.

Table 1 Structural data of MCM-41 before calcination, after calcination, and SSD/MCM-41.

Sample	2θ (°)	Intensity (count)	Relative Crystallinity [(a)] (%)	d_{100} (nm)	a_o [(b)] (nm)	D_{XRD} [(c)] (nm)
MCM-41 before calcination	2.24	26,932	99.7	3.94	4.55	3.55
MCM-41 after calcination	2.21	33,936	99.8	3.98	4.59	3.59
SSD/MCM-41	2.46	28,632	99.8	3.59	4.14	3.14
Commercial MCM-41	2.33	31,459	99.8	3.79	4.38	3.38

Notes: [(a)] means the value for the best-defined intensity of the sample; [(b)] plane lattice parameter [100] using the formula $a_o = 2d/\sqrt{3}$; and [(c)] the approximate value of the pore diameter, $D_{XRD} = a_o - 1$ (nm), assuming that the wall thickness of pore was relatively stable (1nm).

FTIR spectra confirmation in MCM-41 preparation and changes after solasodine adsorption

The FTIR spectra before calcination in **Figure 3(A)** show that the variation of sonication time affects the structure of MCM-41. The O–H stretching vibration shifted from 3,427 to 3,424 cm^{-1} with increasing sonication time (30 - 150 min), indicating stronger hydrogen bonding interactions among silanol (≡Si–OH) groups and thus an increased abundance of surface silanol. The C–H band (2,920 - 2,851 cm^{-1}) of surfactant CTAB decreases, indicating enhanced surfactant release efficiency with greater sonication times. The Si–O–Si characteristic band (1,060 - 1,069 cm^{-1}) slightly shifts to reveal the periodicity of the mesoporous structure. Symmetrical stretching Si–O (795 - 797 cm^{-1}) and bending Si–O (457 - 455 cm^{-1}) vibrational bands remain unchanged, indicating that the silica mainframe remains intact. The similar FTIR spectra of MCM-41 have also been reported [19].

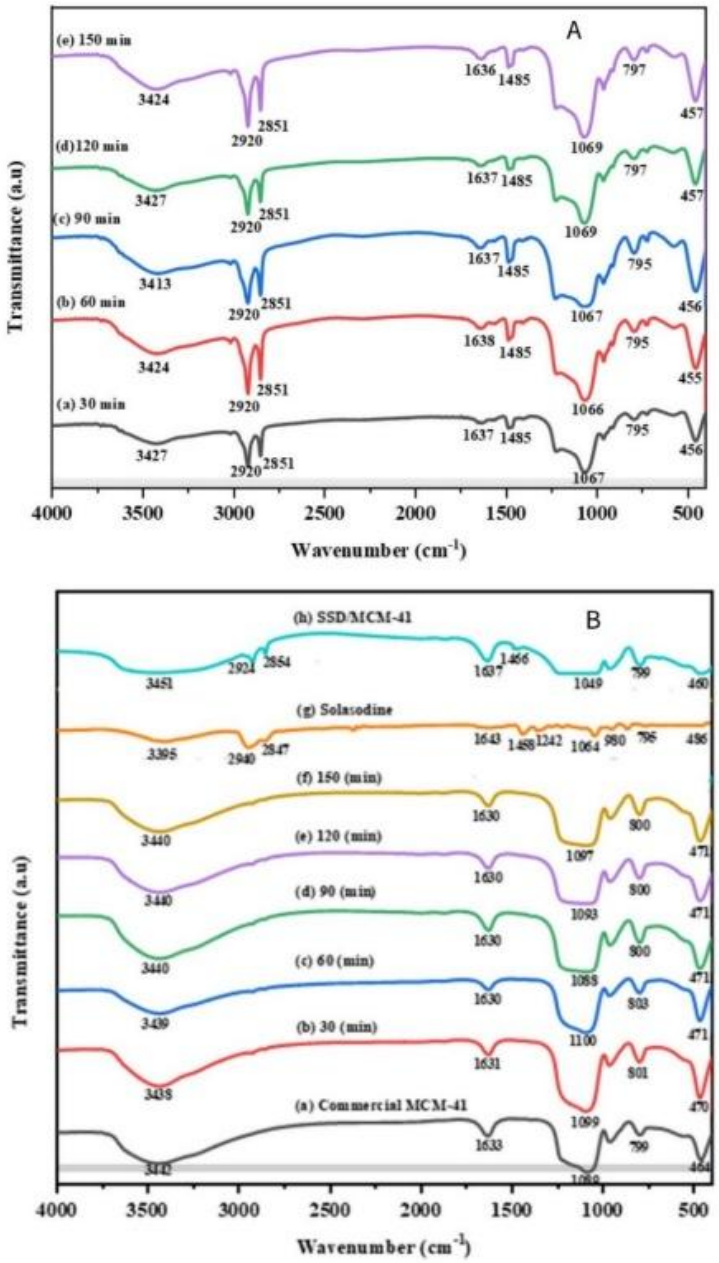

Figure 3 (A) FTIR spectra of MCM-41 before calcination with a variation of sonication time; (B) FTIR spectra of Commercial MCM-41, MCM-41 after calcination with a variation of sonication time, solasodine, and MCM-41 after being used to adsorb solasodine (SSD/MCM-41).

The FTIR spectra of MCM-41 calcined for various sonication times (30 - 150 min), shown in **Figure 3(B)**, exhibit the characteristic features of mesoporous silica. The absorption band at 3,440 - 3,451 cm^{-1} due to the O–H stretching vibration of ≡Si–OH groups and adsorbed water decreases with sonication time, suggesting greater silica network condensation due to the ≡Si–OH polycondensation reaction. The absorption band at 3,440 - 3,451 cm^{-1} is caused by the ≡Si–OH and adsorbed water O–H stretching vibration. The 3,451 cm^{-1} band shifted to 3,440 cm^{-1} upon solasodine loading, caused by hydrogen bonding interactions between solasodine hydroxyl groups and surface silanol groups of MCM-41. This indicates the adsorption of solasodine onto the silica matrix. The structural integrity of MCM-41 is not disturbed by calcination and sonication, as confirmed by the presence of Si–O–Si asymmetric stretching (1,088 - 1,097 cm^{-1}), symmetric stretching

(800 - 803 cm^{-1}), and Si–O deformation (471 cm^{-1}). The lack of bands at 2,925 and 2,854 cm^{-1} for the C–H stretching vibrations of CTAB confirms the removal of the organic template. In the case of the commercial MCM-41 used as the control, there are negligible shifts and intensity variations, namely at 1,088 - 1,097 cm^{-1}, corresponding to pore ordering change and density of the residual ≡Si–OH groups caused by sonication. These structural variations may be accountable for improved material stability, which may promote framework stability and function performance.

After loading solasodine, FTIR spectrum of SSD/MCM-41showed new peaks at 2,924 and 2,854 cm^{-1} (C–H stretching), 1,466 cm^{-1} (C–H bending), and 1,049 cm^{-1} (C–O–C stretching of solasodine shifted from 1,064 cm^{-1}), confirming the adsorption of solasodine on the mesoporous framework. The adsorption of solasodine on MCM-41 is evidenced from the shift in the O–H stretching vibration from 3,451 to 3,440 cm^{-1} and the O–H bending from 1,637 to 1,630 cm^{-1}. The shifts confirm hydrogen bonding interaction between the hydroxyl of solasodine and the silanol groups (≡Si–OH) of MCM-41, confirming successful adsorption without breaking the silica framework. The alteration suggests interactions through hydrogen bonds between the ≡Si–OH groups of MCM-41 and hydroxyl (–OH) groups of solasodine, in addition to possible interactions involving its heterocyclic (–NH) moiety. The unchanged Si–O–Si stretching band at ~1,097 cm^{-1} directly proves that the silica framework is not disturbed, again confirming that solasodine adsorption occurs without causing any structural damage to the mesoporous host matrix.

The interaction of the silanol groups of MCM-41 and the hydroxyl or amino groups of solasodine, as proven by the O–H band shift, shows hydrogen bonding which enhances drug–matrix affinity. These interactions can prevent drug leaching early on and consolidate the loaded system stability.

SEM image of MCM-41 and SSD/MCM-41

SEM analysis was conducted at 5,000× magnification to observe the morphology and surface texture of the synthesized materials, as shown in **Figure 4**: (A) MCM-41 before calcination, (B) MCM-41 after calcination, (C) SSD/MCM-41, and (D) commercial MCM-41 used as the control. The relatively uniform spherical aggregates observed in **Figure 4** are the consequence of ordering silica around CTAB micelles during preparation. Ultrasonic irradiation facilitates dispersion and nucleation regularity of the micelles to create mesoporous siliceous particles of regular morphology characteristic of MCM-41. Before calcination, MCM-41 had rough surfaces with unordered pores characteristic of residual organic templates. After calcination, an ordered mesoporous structure was observed, showing removal of surfactant and stable framework development. Solasodine loading caused the blocking of pores partially and surface aggregation, but the mesoporous structure was fairly well preserved, evidencing scope for controlled release.

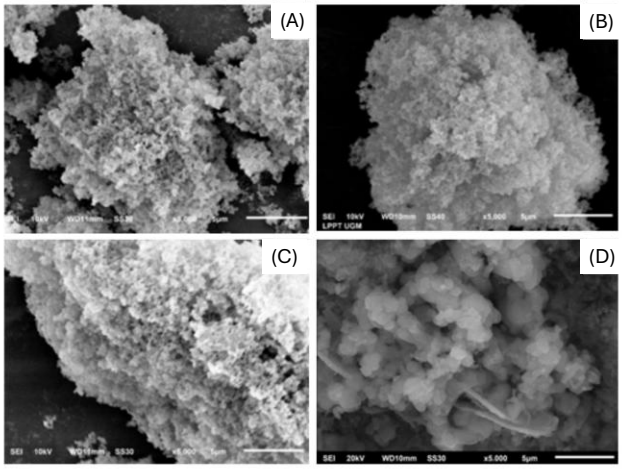

Figure 4 SEM images with 5,000 times magnification (A) MCM-41 before calcination, (B) MCM-41 after calcination, (C) SSD/MCM-41, and (D) Commercial MCM-41.

EDX of MCM-41 and SSD/MCM-41

EDX spectroscopy was used to recognize the elemental constitution of the samples, as revealed in **Figure 5**. The EDX spectrum of the uncalcined MCM-41 shows a very high carbon content (18.95%), which indicates the presence of residual organic surfactants, primarily CTAB, within the silica framework. After calcination, the content of carbon decreases remarkably to 6.16%, which confirms the effective elimination of the organic template through thermal treatment at high temperatures. Meanwhile, the oxygen and silicon contents are raised, indicating the formation of a more compact and pure silica network. In the SSD/MCM-41 composite, there is a slight increase in the carbon content to 9.18%, which is attributed to the successful loading of solasodine, an organic compound. The enhancement of silicon content to 50.03% after solasodine loading verifies that the silica structure of MCM-41 is chemically unaltered. Since solasodine merely interacts with silanol groups on the surface and not with the Si–O–Si backbone, the mesoporous architecture is well retained. The stability indicates its possible function as a potent drug delivery system.

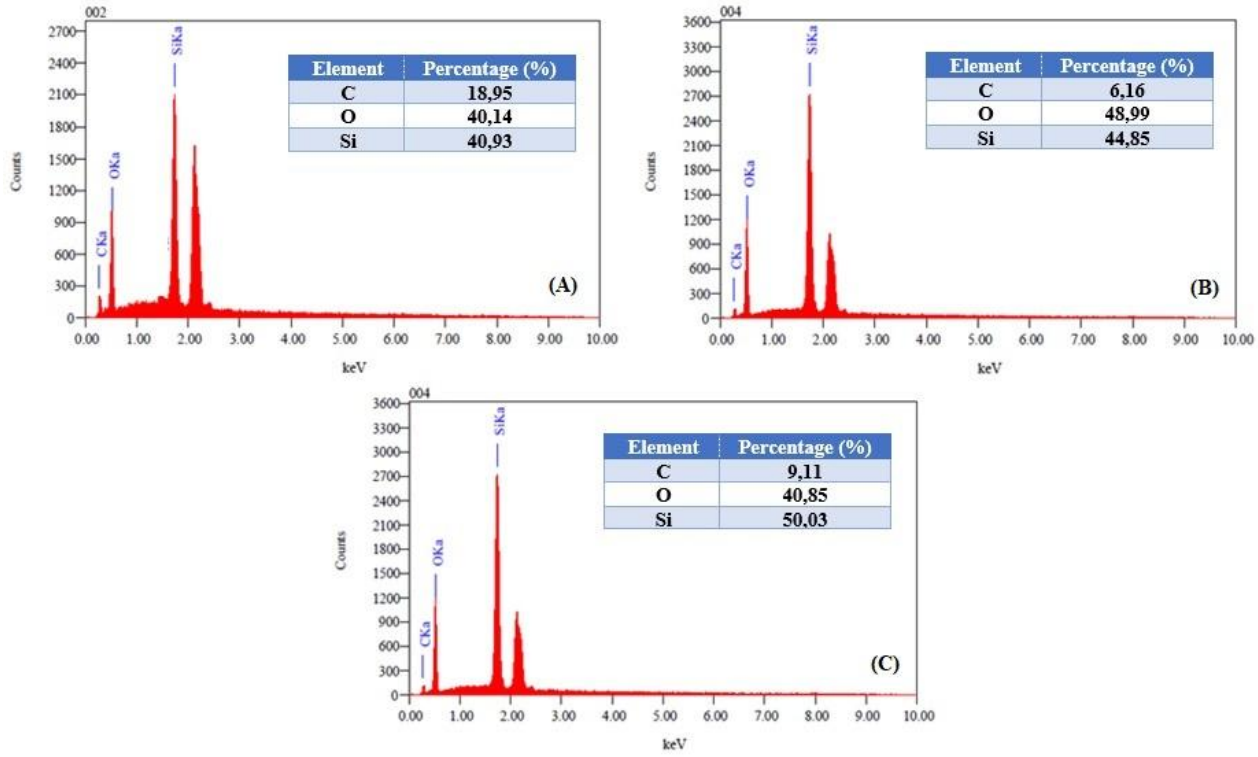

Figure 5 EDX (A) MCM-41 before calcination, (B) MCM-41 after calcination and (C) SSD/MCM-41.

TEM image of MCM-41 and SSD-MCM-41

TEM image (**Figure 6**) indicated that as-prepared MCM-41 consisted of aggregated, spherical particles with visible mesoporous structures. In loading solasodine, increased contrast of the image and partial pore blocking indicated effective adsorption of solasodine into the silica matrix without compromising the mesostructure. Commercial MCM-41 used as the control had well-ordered and well-arranged pores due to its optimized preparation and calcination processes under controlled industrial conditions. The enhanced ordering is a benchmark against which the quality of laboratory-prepared MCM-41 is compared.

The spherical morphology and monodisperse particle size observed under SEM and TEM are advantageous for drug delivery due to ease of homogeneous dispersion in biological fluids and reproducible release kinetics. The uniformity in structure also avoids burst release and enables reproducible adsorption–desorption behavior.

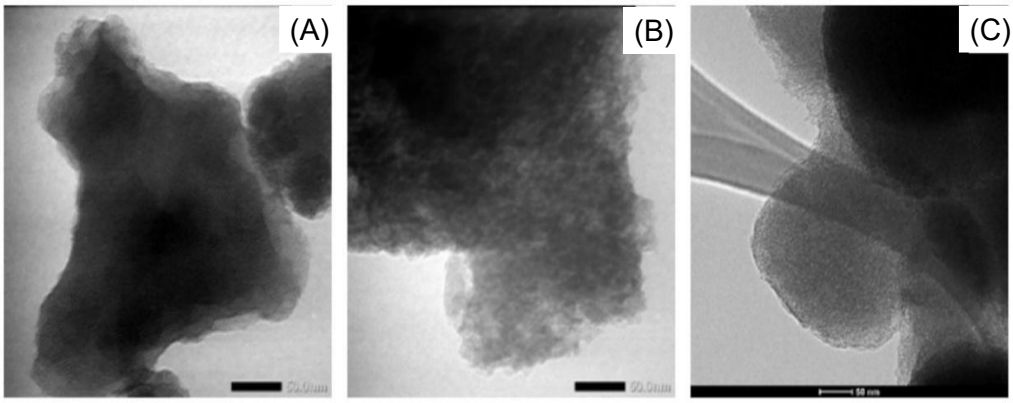

Figure 6 TEM image (A) MCM-41, (B) SSD/MCM-41 and (C) Commercial MCM-41.

N_2 adsorption-desorption

The nitrogen adsorption-desorption isotherm presented in **Table 3** reflects significant variations in the textural characteristics of MCM-41 when loaded with solasodine. The pure MCM-41 showed an extremely high specific surface area (1,129.39 m^2/g), accompanied by a pore volume of 0.87 cc/g and a pore diameter of 3.41 nm. Such textural features are typical for highly ordered MCM-41, suggesting that there was efficient removal of CTAB surfactant templates and generation of accessible mesoporous channels with an abundance of active sites accessible for adsorption of drugs. Upon solasodine loading, SSD/MCM-41 displays a prominent decrease in S_{BET} to 849.31 m^2/g, V_p to 0.59 cc/g, and D_{BJH} to 2.18 nm, which indicates effective adsorption and partial mesopore filling with solasodine molecules. A marginal reduction in the unit cell dimension (a_o) from 4.59 to 4.14 nm, along with an augmentation of the pore wall thickness (W_t) from 1.18 to 1.96 nm, supports the hypothesis even more that solasodine is successfully trapped inside the mesoporous channels, resulting in a diminished pore structure without any loss of hexagonal ordering. These results confirm the application of MCM-41 as a carrier for solasodine. Decreases in surface area and pore size confirm the successful loading of solasodine into the mesopores, while the increase in wall thickness indicates the strengthening of the structure of the silica framework. This blend is useful for ensuring stability and regulating the release kinetics of solasodine in controlled drug delivery.

Reduction in surface area and pore volume on solasodine loading establishes successful drug molecule encapsulation within the mesopores. As the accessible surface decreases, residual porosity is responsible for gradual solvent penetration to promote sustained and controlled drug release.

Table 2 Physical Properties of MCM-41 and SSD/MCM-41.

Sample	S_{BET}[a)] (m^2/g)	Vp[b)] (cc/g)	D_{BJH}[c)] (nm)	a_o [d)] (nm)	W_t[e)] (nm)
MCM-41	1,129.39	0.87	3.41	4.59	1.18
SSD/MCM-41	849.31	0.59	2.18	4.14	1.96

Description: [a)] specific surface area, [b)] pore volume, [c)] pore diameter, calculated based on the BJH model of adsorption pathway, [d)] unit cell, and [e)] pore wall thickness, calculated by the formula $W_t = a_o - D_{BJH}$

Adsorption of solasodine

Effect of pH

pH is an important parameter that affects adsorption since pH will influence the surface charge of the adsorbent and the protonation-deprotonation of the adsorbate. For the adsorbent of MCM-41, its pH_{PZC} determination, as a tool for predicting the surface charge, along with its ability to adsorb solasodine, are presented in **Figure 7**. The pH_{PZC} provides information about the balance between the positive and negative charges on the surface [40]. pH_{PZC} measurement in this study was performed by the salt addition method [41].

The pH_{PZC} of MCM-41 is ≈ 5 (**Figure 7**), meaning that the MCM-41 is positively charged at pHs below 5 and oppositely is negatively charged at pHs higher than 5. At a pH range below the pH_{PZC}, surface ≡Si–OH of MCM-41 should be protonated to ≡Si–OH_2^+, meanwhile solasodine is mostly neutral since its *pKa* is 7.7 [42].

As observed in **Figure 7**, the adsorption of solasodine increased with pH, starting from pH 1 and reaching a maximum at pH 4, before decreasing sharply at pH > 5. Although the surface remains positive in the pH range of 1 - 4, the density of positive charge reduces with pH because surface silanol groups undergo stepwise deprotonation (≡Si–OH → ≡Si–O^-). Lower charge density facilitates greater hydrogen bonding between MCM-41 silanol groups and –OH or –NH groups of solasodine, thus enhancing adsorption at pH 4.

When the pH exceeds the pH_{PZC}, the surface ≡Si–OH groups of MCM-41 are progressively deprotonated to ≡Si–O^-, increasing the negative surface charge density. At the same time, solasodine molecules undergo greater deprotonation of their –OH groups at alkaline pH, leading to an increase in their net negative charge. The combination of a more negatively charged MCM-41 surface and more negatively charged solasodine intensifies electrostatic repulsion, which becomes stronger with increasing pH and consequently reduces the adsorption ability. Therefore, the optimum pH for adsorption is pH 4, where the balance between positive surface charge and hydrogen bonding interactions is most favorable.

The highest adsorption at pH 4 can therefore be understood by considering both the *pKa* of solasodine (≈7.7) and the surface charge behavior of MCM-41 (pH_{PZC} ≈ 5). MCM-41 remains protonated to some degree at pH 4, but with decreasing positive charge density, which prefers hydrogen bonding interactions between MCM-41 silanol groups and –OH or –NH groups of the undeprotonated solasodine rather than strong electrostatic repulsion. Equilibrium between reduced positive surface charge on MCM-41 and appropriate points of interaction on solasodine is responsible for pH 4 being the best condition for adsorption. In elevated pH values (> 5), both silica surface and solasodine molecules carry a greater negative charge, resulting in electrostatic repulsion and a substantial reduction in adsorption. Although pH 4 is physiologically irrelevant, it was selected as the optimal experimental condition for the adsorption study to specify the underlying interaction processes. Further investigations, including release and cytotoxicity under physiological pH (≈7.4), are planned to determine its biological appropriateness.

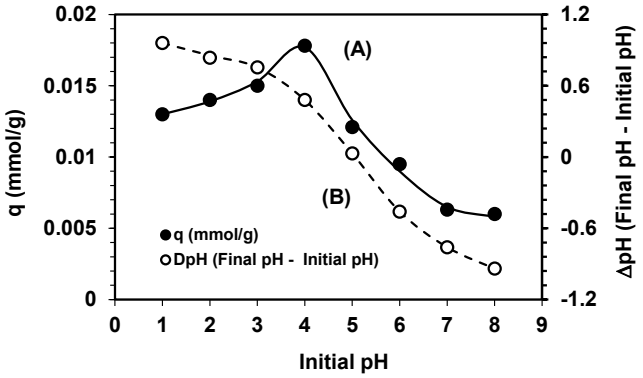

Figure 7 (A) Effect of solution pH on the adsorption of solasodine on MCM-41, (B) pH_{PZC} determination.

The effect of contact time and the determination of adsorption kinetics

When the pH exceeds the pH_{PZC}, the surface ≡Si–OH groups of MCM-41 are progressively deprotonated to ≡Si–O^-, increasing the negative surface charge density. At the same time, solasodine molecules undergo greater deprotonation of their –OH groups at alkaline pH, leading to an increase in their net negative charge. The combination of a more negatively charged MCM-41 surface and more negatively charged solasodine intensifies electrostatic repulsion, which becomes stronger with increasing pH and consequently reduces the adsorption ability. Therefore, the optimum pH for adsorption is pH 4, where the balance between

positive surface charge and hydrogen bonding interactions is most favorable.

The ability of MCM-41 in adsorbing solasodine (q_t) increases with increasing time until equilibrium is achieved at ≈ 90 min (**Figure 8(A)**). In the first step (0 - 45 min), the adsorption increases sharply. At 60 min, the adsorption rate starts decreasing because there are fewer remaining active sites for adsorption. The q_t value is relatively stable between 90 - 150 min, which indicates equilibrium adsorption has been established, and adsorption and desorption rates are equal to each other. Rapid attainment of equilibrium within 90 min is evidence of the strong affinity of MCM-41 towards solasodine because the majority of the active sites were occupied at once, and then the system possessed a steady adsorption capacity.

The adsorption data presented in **Figure 8(A)** were further analyzed using the pseudo-first order (Eq. (1)), pseudo-second order (Eq. (2)), and second order reaching equilibrium (Eq. (3)) kinetic models, with the results shown in **Figures 8(B) - 8(D)**, respectively. It can be observed that the second-order reaching equilibrium kinetic model provides the best fit to the experimental data, with a correlation coefficient (R^2) = 0.996, while the pseudo-first and pseudo-second order models yield comparable R^2 values. The second-order reaching equilibrium kinetic model is formulated based on the concentration of solasodine remaining in the solution, whereas the pseudo–first and pseudo-second order models are based on the amount of solasodine adsorbed on the adsorbent. Therefore, the fact that the second-order reaching equilibrium model better describes the data in **Figure 8(A)** suggests that the loss of solasodine from the solution is not governed solely by adsorption.

The results of the adsorption data analysis from **Figure 8(A)** using the 3 kinetic models described above are summarized in **Table 4**. Although both the pseudo-first-order and pseudo-second-order models produced comparable R^2 values, the qe value predicted by the pseudo-first-order model (0.95×10^{-2} mmol/g) was significantly lower than the experimental result (0.12 mmol/g, **Figure 8(A)**), indicating its limitations in describing the overall adsorption process. In contrast, the pseudo-second-order model yielded a q_e value (1.18×10^{-2} mmol/g) that was very close to the experimental result, suggesting that chemisorption is the dominant mechanism. Thus, it appears that the removal of solasodine from the solution is primarily governed by chemisorption, which reflects the strong interaction between solasodine and the optimized MCM-41 surface. This finding enhances the potential of the synthesized MCM-41 as a reliable and effective delivery system for solasodine.

The good model fit for the second-order equilibrium model suggests that adsorption is not controlled by diffusion but by particular molecular interactions. Indeed, solasodine possesses hydroxyl and amino functional groups to form hydrogen bonds and electrostatic interactions with the silanol surface groups of MCM-41, consistent with a chemisorption mechanism. At the same time, the big steroidal hydrophobic backbone of solasodine can bind in the mesoporous channels by van der Waals forces and hydrophobic forces, implying that physisorption is also involved in the initial rapid adsorption. Therefore, even the solasodine adsorption on MCM-41 can be reasoned as a synergistic process where chemisorption is dominant and physisorption assists in the initial period.

Table 3 The rate constants for the pseudo-first (k_{1p}), pseudo-second (k_{2p}), and second orders reaching equilibrium (k_2) for the solasodine adsorption on MCM-41.

Kinetics model	Parameters	Parameters value
Pseudo-first order [a)]	k_{1p} (10^{-2} min^{-1})	4.31
	q_e (10^{-2} mmol/g)	0.95
	R^2	0.993
Pseudo-second orde [b)]	k_{2p} (g/mmol min)	4.44
	q_e (10^{-2} mmol/g)	1.18
	R^2	0.992
Second order reaching equilibrium [c)]	k_2 (L/mmol min)	0.571
	R^2	0.996

[a)] Originated by Lagergren [36]; [b)] Formulated by Ho and McKay [37]; [c)] Proposed by Santosa [38].

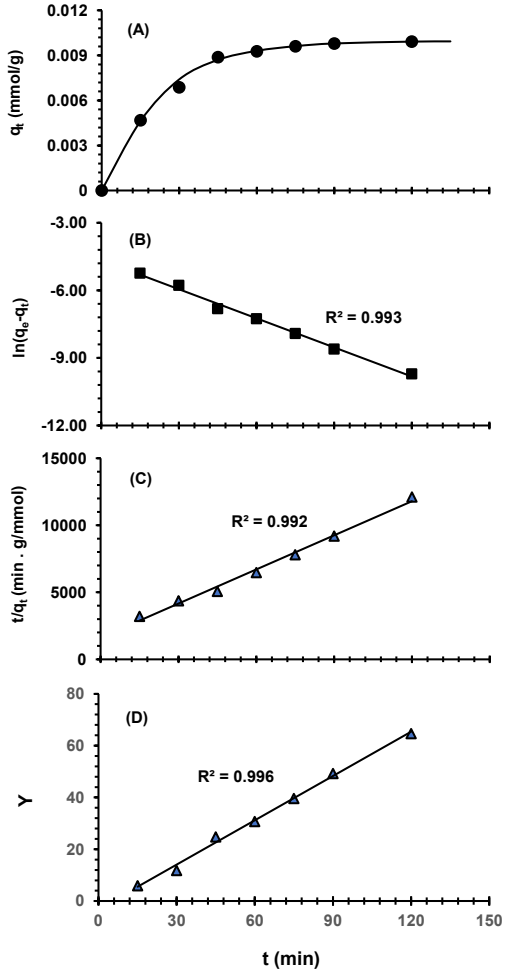

Figure 8 (A) Adsorption profile of solasodine on MCM-41 at different contact times, and the corresponding kinetic model analyses: (B) pseudo-first order, (C) pseudo-second order, and (D) second order reaching equilibrium. The symbol Y is introduced as a representation for $\frac{1}{C_e}[\ln\left\{\frac{C_t(C_0-C_e)}{C_0(C_t-C_e)}\right\}]$.

The effect of concentration and the determination of the adsorption isotherm

The relationship between the solasodine concentration at equilibrium (C_e) and the amount of solasodine adsorbed at equilibrium (q_e) is presented in **Figure 9**. The value of q_e increases rapidly by increasing C_e up to 0.06 mmol/L, then rises more slowly until C_e reaches 0.28 mmol/L, after which qe becomes relatively constant at C_e values above 0.28 mmol/L.

Figure 9 also shows the fitting results of experimental data using the Langmuir (Eq. (4)), the Freundlich (Eq. (5)), and the Temkin isotherm models (Eq. (6)) [38,41,43]. The Langmuir isotherm model assumes that adsorption occurs on an energetically homogeneous surface, forming a monolayer of adsorbate molecules without lateral interaction or mobility. In this model, adsorption is considered to take place at specific sites on the surface. The adsorption capacity (q_m) and adsorption intensity (K_L) parameters can be determined from the slope and intercept of the linear plot of C_e/q_e versus C_e, as expressed in Eq. (4).

In contrast to the Langmuir isotherm model, the Freundlich isotherm model describes adsorption on heterogeneous surfaces and allows for the formation of multiple adsorption layers. From Eq. (5), the parameters of adsorption capacity (K_F) and adsorption intensity (n) can be obtained from the intercept and slope of the plot of log q_e versus log C_e, respectively. Meanwhile, the Temkin isotherm model considers the effects of indirect interactions between the adsorbent and adsorbate. The Temkin parameter of equilibrium binding constant (K_T) and parameter related to the heat of adsorption (b_T) can be calculated using Eq. (6) from the slope and intercept of the linear plot of q_e versus ln C_e.

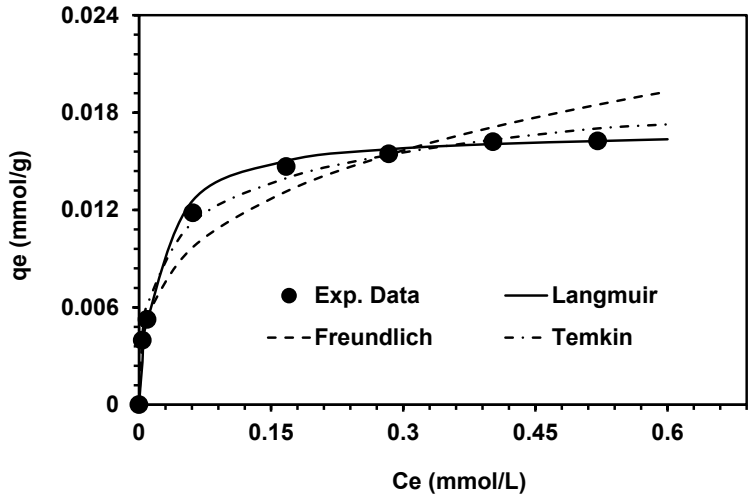

Figure 9 Profile of the equilibrium concentration of solasodine remaining in solution (C_e) against the amount of solasodine adsorbed on MCM-41 (q_e), along with the modeling results of q_e at the existing C_e values using 3 different adsorption isotherm models.

Table 4 The Langmuir's capacity (q_e) and equilibrium constant (K_L), as well as the Freundlich's capacity (K_F) for the solasodine adsorption by the MCM-41.

Isotherm model	Parameters	Value parameter
Langmuir	q_e (10^{-2} mmol/g)	1.69
	K_L (L/mmol)	47.93
	R^2	0.999
Freundlich	K_F (10^{-2} mmol/g)	2.25
	n	3.33
	R^2	0.963
Temkin	b_T (kJ/mol)	917.63
	K_T (L/g)	1053.63
	R^2	0.986

As shown clearly in **Figure 9**, the Langmuir model provides the best fit to the experimental data compared to the other 2 models. The parameters obtained from fitting the data with the 3 isotherm models are summarized in **Table 5**. The excellent agreement of the Langmuir isotherm model with the experimental data is evidenced by its correlation coefficient (R^2 = 0.999), which is closer to unity than those obtained from the Freundlich (R^2 = 0.963) and Temkin (R^2 = 0.986) models. Application of the Langmuir isotherm yielded an adsorption capacity (q_e) of solasodine on MCM-41 of 1.69×10^{-2} mmol/g and an adsorption intensity (K_L) of 47.89×10^3 L/mol. Using the adsorption energy relation $E_{ads} = -RT \ln K_L$ [44], the adsorption energy was calculated to be 26.70 kJ/mol. Previous studies have reported that adsorption energies of this magnitude are typical of adsorbate-adsorbent interactions governed by hydrogen bonding [45]. It would, therefore, be reasonable to assume that MCM-41 possesses relatively homogeneous surface energy, where the adsorption energy remains constant regardless of the degree of surface coverage. Once solasodine is adsorbed, it does not undergo lateral interaction or mobility.

Although the adsorption of solasodine onto MCM-41 (1.69×10^{-2} mmol/g) is lower than that of curcumin onto mesoporous silica carriers [31], it is because of their molecular structures and physicochemical properties. Curcumin is a polyphenolic compound with multiple hydroxyl groups, which enables strong hydrogen bonding and also π–π interactions with the

silica matrix, resulting in higher adsorption. On the other hand, solasodine is a steroidal alkaloid with a bulky hydrophobic backbone, which lowers the amount of available adsorption sites. Solasodine, nonetheless, has been reported to possess high anticancer activity, in which biomedical efficacy can be achieved at low doses, indicating that high adsorption capacity is not the sole parameter that dictates biomedical performance. Significantly, the MCM-41 matrix in the current study remained structurally stable after solasodine loading, and the adsorption process followed a Langmuir monolayer model, thus ensuring controlled and predictable drug loading and release. Collectively, these findings are indicative of the novelty of SSD/MCM-41 as a stable and selective nanocarrier system, differing from other alkaloid-based delivery systems.

Proposed mechanism of solasodine adsorption and controlled release

As shown the FTIR spectra in **Figure 3B(h)** for SSD/MCM-41, after solasodine adsorption, shift of O–H stretching band from 3,451 to 3,440 cm^{-1} and O–H bending from 1,637 to 1,630 cm^{-1} were observed, indicating the presence of weak hydrogen bonding or polarity alteration for ≡Si–OH functional groups of MCM-41. The modification suggests the presence of hydrogen bonds between the ≡Si–OH groups of MCM-41and mainly –OH groups of solasodine, in addition to possible interactions involving its heterocyclic (–NH) moiety. The unchanged Si–O–Si stretching band at ~1,097 cm^{-1} directly proves that the silica framework is not disturbed, again confirming that solasodine adsorption occurs without causing any structural damage to the mesoporous host matrix. This suggestion is further supported by the measured adsorption energy of 26.70 kJ/mol as mentioned above, which falls within the range of hydrogen bonding energies [43]. Based on all this information, the interaction model between MCM-41 and solasodine is illustrated in **Figure 10**.

Thus, the adsorption of solasodine onto MCM-41 is primarily governed by hydrogen bonding between the –OH groups of solasodine and, to a lesser extent, its heterocyclic –NH groups, with the surface ≡Si–OH groups of MCM-41. These interactions are strong enough to retain solasodine within the carrier system, yet sufficiently weak to enable its gradual release under physiological conditions [19].

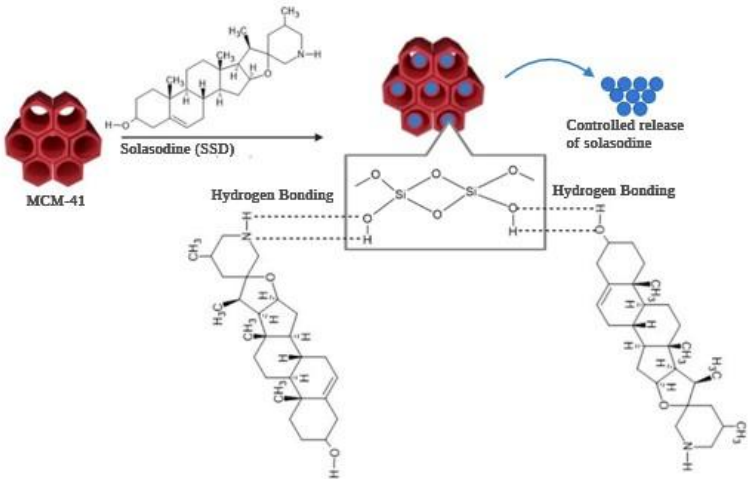

Figure 10 Proposed schematic of solasodine adsorption and release mechanism on MCM-41. Solasodine molecules will be bound to silanol groups (≡Si–OH) of MCM-41 by hydrogen bonding during loading, which will lead to a stable association within the mesopores. Solasodine is released slowly by diffusion under aqueous conditions, yielding controlled drug delivery.

A schematic representation of the loading and release process of solasodine in the mesoporous MCM-41 matrix is shown in **Figure 10**. During loading, the solasodine molecules are interacting with silanol groups (≡Si–OH) at the inner pore surfaces through hydrogen bonding and weak van der Waals forces, leading to homogeneous distribution within the hexagonal channels. Upon exposure to release medium, solvent

molecules infiltrate the pores, gradually substituting solasodine via diffusion-controlled desorption. The structural stability of MCM-41 and its narrow pore distribution act to facilitate a prolonged release profile, minimizing premature drug loss and improving potential therapeutic performance.

This research is limited to physicochemical characterization and adsorption experiments, with no biological verification. Absence of *in vitro* release and cytotoxicity at this time limits biological extrapolation of data. Our present studies in the laboratory are focused on elucidating the release kinetics and anticancer efficacy of solasodine-loaded MCM-41 in cell models to further confirm its use as a targeted drug carrier.

Overall, these structural and textural properties present that the surface of the prepared MCM-41 is stable and biocompatible and can serve as a platform to host solasodine molecules well with properties very apt for sustained and target drug delivery applications.

Conclusions

This study demonstrates the potency of MCM-41 as a solasodine carrier through structural, morphological, and adsorption analyses. XRD analysis confirmed a highly ordered hexagonal mesoporous structure retained after solasodine adsorption, despite reduced peak intensity. FTIR spectra revealed hydrogen bonding between MCM-41's ≡Si–OH groups and solasodine's –OH groups and heterocyclic (–NH), enabling solasodine retention and controlled release. TEM and SEM analyses showed intact morphology with partial pore blockage, indicating successful adsorption. BET analysis supported these findings, showing decreases in surface area (from 1,129.39 to 849.31 m^2/g), pore volume (from 0.87 to 0.59 cc/g), and pore diameter (from 3.41 to 2.17 nm). Adsorption was optimum at pH 4.0, followed kinetics model of second order reaching equilibrium, and the Langmuir isotherm model with an adsorption capacity of 1.69×10^{-2} mmol/g and adsorption energy of 26.70 kJ/mol. Overall, MCM-41 possesses excellent structural stability and adsorption ability, and hence suggests it as a promising carrier of solasodine in targeted anticancer drug delivery. Further biological assessment, including *in vitro* release and cytotoxicity experiments, needs to be done to delineate its therapeutic value.

Acknowledgements

The authors acknowledge with gratitude the Indonesian Endowment Fund for Education (LPDP), the Indonesian Education Scholarship (BPI), the Center for Higher Education Funding and Assessment, the Ministry of Higher Education, Science, and Technology of the Republic of Indonesia (PPAPT) for providing PhD scholarship and study fund for the first author through decision letter No.1878/J5.2.3./BPI.06/10/2021.

Declaration of Generative AI in Scientific Writing

The authors acknowledge the use of generative AI tools (e.g., QuillBot and ChatGPT by OpenAI) in the preparation of this manuscript, specifically for language editing and grammar correction. No content generation or data interpretation was performed by AI. The authors take full responsibility for the content and conclusions of this work.

CRediT Author Statement

Rohmatun Nafi'ah: Data curation, Formal analysis, Investigation, Resources, Visualization, Writing - original draft. **Sri Juari Santosa:** Conceptualization, Methodology, Supervision, Validation, Writing - review & editing. **Sutarno Sutarno:** Conceptualization, Methodology, Supervision, Writing - review & editing. **Eti Nurwening Sholikhah:** Conceptualization, Methodology, Supervision.

References

[1] H Guo, X Zhao, Y Duan and J Shi. Hollow mesoporous silica nanoparticles for drug formulation and delivery: Opportunities for cancer therapy. *Colloids and Surfaces B: Biointerfaces* 2025; **249**, 114534.

[2] J Liu, J Liu, Y Wang, F Chen, Y He, X Xie, Y Zhong and C Yang. Bioactive mesoporous silica materials-assisted cancer immunotherapy. *Biomaterials* 2025; **315**, 122919.

[3] AK Singh, S Singh, T Minocha, SK Yadav, R Narayan, UY Nayak, SK Singh and R Awasthi. *In vitro* profiling and molecular dynamics simulation studies of berberine-loaded MCM-41 mesoporous silica nanoparticles to prevent neuronal apoptosis. *Nanoscale Advances* 2024; **6(9)**, 246-2486.

[4] S Batool, S Sohail, FU Din, AH Alamri, AS Alqahtani, MA Alshahrani, MA Alshehri and HG Choi. A detailed insight of the tumor targeting using nanocarrier drug delivery system. *Drug Delivery* 2023; **30(1)**, 2183815.

[5] P Kolimi, S Narala, AAA Youssef, D Nyavanandi and N Dudhipala. A systematic review on development of mesoporous nanoparticles as a vehicle for transdermal drug delivery. *Nanotheranostics* 2023; **7**, 70-89.

[6] Z Li, L Liu, Z Wang, P Gao and GK Li. Synthesis and application of mesoporous materials: Process status, technical problems and development prospects: A mini-review. *Energy & Fuels* 2023; **37(5)**, 3413-3427.

[7] R Foulady-Dehaghi, S Sohrabnezhad and M Hadavi. Drug delivery with solvent-free synthesized polyimide-COF/amino-functionalized MCM-41 nanohybrid. *Journal of Drug Delivery Science and Technology* 2023; **81**, 104283.

[8] R Narayan, S Gadag, S Garg and UY Nayak. Understanding the effect of functionalization on loading capacity and release of drug from mesoporous silica nanoparticles: A computationally driven study. *ACS Omega* 2022; **7(10)**, 8229-8245.

[9] K Djayanti, P Maharjan, KH Cho, S Jeong, MS Kim, MC Shin and KA Min. Mesoporous silica nanoparticles as a potential nanoplatform: Therapeutic applications and considerations. *International Journal of Molecular Sciences* 2023; **24(7)**, 6349.

[10] A Ojha, S Jaiswal, P Bharti and SK Mishra. Nanoparticles and nanomaterials-based recent approaches in upgraded targeting and management of cancer: A review. *Cancers* 2023; **15(1)**, 162.

[11] M Deinavizadeh, A Kiasat, N Hooshmand, M Shafiei, M Sabaeian, R Mirzajani, SM Zahraei, HI Labouta and MA El-Sayed. Smart NIR-light and pH-responsive doxorubicin-loaded GNRs@SBA-15-SH nanocomposite for chemo-photothermal therapy of cancer. *Nanophotonics* 2021; **10(12)**, 3303-3319.

[12] ZH Mahmoud, UAR Hussein, AM Dhiaa, AF Al-Hussainy, N Aljbory, MH Shuhata, MJ Alnajar, DK Aljaberi, ASOK Khawaf, DK Mahapatra, E Kianfar, TM Joseph and S Thomas. Nano-based drug delivery in cancer: Tumor tissue characteristics and targeting. *Trends in Sciences* 2025; **22(2)**, 9078.

[13] L Sun. Smart nanoparticles for cancer therapy. *Signal Transduction and Targeted Therapy* 2023; **8**, 418.

[14] S Swami. Nanomaterial catalyzed green synthesis of tetrazoles and its derivatives: A review on recent. *RSC Advances* 2021; **11**, 39058-39086.

[15] YW Lin, WH Lee, CY Chen, YJ Liu, WQ Zhang, MY Lin and KL Lin. Synthesis of aluminum-mesoporous MCM-41 humidity control material from thin-film transistor liquid crystal display waste glass and sandblasting waste and its application. *Boletín de la Sociedad Española de Cerámica y Vidrio* 2023; **62(4)**, 357-367.

[16] A Corma, P Botella and E Rivero-Buceta. Silica-based stimuli-responsive systems for antitumor drug delivery and controlled release. *Pharmaceutics* 2022; **14(1)**, 110.

[17] M Hachemaoui, CB Molina, C Belver, J Bedia, A Mokhtar, R Hamacha and B Boukoussa. Metal-loaded mesoporous MCM-41 for the catalytic wet peroxide oxidation (CWPO) of acetaminophen. *Catalysts* 2021; **11(2)**, 219.

[18] K Abouaitah and W Lojkowski. Delivery of natural agents by means of mesoporous silica nanospheres as a promising anticancer strategy. *Pharmaceutics* 2021; **13(2)**, 143.

[19] Z Shariatinia, N Pourzadi and SMR Darvishi. Tert-butylamine functionalized MCM-41 mesoporous nanoparticles as drug carriers for the controlled release of cyclophosphamide anticancer drug. *Surfaces and Interfaces* 2021; **22**, 100842.

[20] GD Aquino, MS Moreno, CM Piqueras, GP Benedictto and AM Pereyra. Alternative synthesis of MCM-41 using inexpensive precursors for CO_2 capture. *Inorganics* 2023; **11(12)**, 480.

[21] C de la Torre, R Gavara, A García-Fernández, M Mikhaylov, MN Sokolov, JF Miravet, F Sancenón, R Martínez-Máñez and F Galindo. Enhancement of photoactivity and cellular uptake of $(Bu_4N)_2[Mo_6I_8(CH_3COO)_6]$ complex by loading on porous MCM-41 support. Photodynamic studies as an anticancer agent. *Biomaterials Advances* 2022; **140**, 213057.

[22] C Voycheva, T Popova, M Slavkova, V Tzankova, D Stefanova, D Tzankova, I Spassova, D Kovacheva and B Tzankov. Doxorubicin and quercetin double loading in modified MCM-41 lowered cardiotoxicity in H9c2 cardioblast cells *in vitro*. *Bioengineering* 2023; **10**, 637.

[23] B Tahmasbi, M Nikoorazm, P Moradi and YA Tyula. A Schiff base complex of lanthanum on modified MCM-41 as a reusable nanocatalyst in the homoselective synthesis of 5-substituted 1H-tetrazoles. *RSC Advances* 2022; **12**, 34303-34317.

[24] V Tzankova, D Aluani, Y Yordanov, M Valoti, M Frosini, I Spassova, D Kovacheva and B Tzankov. *In vitro* toxicity evaluation of lomefloxacin-loaded MCM-41 mesoporous silica nanoparticles. *Drug and Chemical Toxicology* 2021; **44(3)**, 238-249.

[25] T Popova. Mesoporous silica MCM-41 and HMS as advanced drug delivery carriers for bicalutamide. *Journal of Drug Delivery Science and Technology* 2021; **62**, 102340.

[26] BTT Luyen. New solasodine-type glycoalkaloids isolated from solanum nigrum and their cytotoxic activity. *Chemical & Biodiversity* 2024; **21(7)**, e202400872.

[27] Y Yang. A combined treatment with Ursolic acid and Solasodine inhibits colorectal cancer progression through the AKT1/ERK1/2-GSK-3β-β-catenin axis. *Phytomedicine* 2024; **135**, 156068.

[28] D Arumuganainar. Exploring the therapeutic role of Solasodine in oral cancer management. *Natural Product Research* 2024. https://doi.org/10.1080/14786419.2024.2408656

[29] Y Alyassin, EG Sayed, P Mehta, K Ruparelia, MS Arshad, M Rasekh, J Shepherd, I Kucuk, PB Wilson, N Singh, MW Chang, DG Fatouros and Z Ahmad. Application of mesoporous silica nanoparticles as drug delivery carriers for chemotherapeutic agents. *Drug Discovery Today* 2020; **25(8)**, 1513-1520.

[30] N Atiyah, M Atiya and T Albayati. Curcumin Loaded onto Magnetic Mesoporous Material MCM-41 for Controlled and Release in Drug Delivery System. *Engineering and Technology Journal* 2022; **40(3)**, 472-483.

[31] NA Atiyah. Functionalization of mesoporous MCM-41 for the delivery of curcumin as an anti-inflammatory therapy. *Advanced Powder Technology* 2022; **33(2)**, 103417.

[32] Y Chen, Y Lu and RJ Lee. Nano encapsulated curcumin: And its potential for biomedical applications. *International Journal of Nanomedicine* 2020; **15**, 3099-3120.

[33] S Bhattacharya and BG Prajapati. Mesoporous silica-based nanoparticles in pharmaceutical sciences: A mini-review. *International Journal of Pharmaceutical Sciences and Nanotechnology* 2020; **13(4)**, 4964-4969.

[34] TAN Dau, VMH Le, TKH Pham, VH Le, SK Cho, TNU Nguyen, TKH Ta and TTV Tran. Surface functionalization of doxorubicin-loaded MCM-41 mesoporous silica nanoparticles by 3-aminopropyltriethoxysilane for selective anticancer effect on A549 and A549/DOX Cells. *Journal of Electronic Materials* 2021; **50(5)**, 2932-2939.

[35] J Chen. Solasodine suppresses MCF7 breast cancer stem-like cells via targeting Hedgehog/Gli1. *Phytomedicine* 2022; **107**, 154448.

[36] S Lagergren. Zur theorie der sogenannten adsorption gelöster stoffe. *Kungliga Svenska Vetenskapsakademiens Handlingar* 1898; **24**, 1-39.

[37] YS Ho. Pseudo-second order model for sorption processes. *Process Biochemistry* 1999; **34**, 451-465.

[38] SJ Santosa, M Hadi, FN Aisyah and Nuryono. A novel utilization of sugarcane bagasse-derived ash to reductively remove gold (III) to gold metal: Energetics, kinetics and mechanism studies. *Case Studies in Chemical and Environmental Engineering* 2024; **10**, 100802.

[39] E Amdeha, RS Mohamed and AS Dhmees. Sonochemical-assisted preparation of ZnS-ZnO/MCM-41 based on blast furnace slag and electric arc furnace dust for Cr (VI) photoreduction. *Ceramics International* 2021; **47(16)**, 23014-23027.

[40] A Putz, M Ciopec, A Negrea and O Grad. Comparison of Structure and adsorption properties of mesoporous silica functionalized with aminopropyl groups by the co-condensation and

the post-grafting methods. *Materials* 2021; **14**, 628.

[41] M Kurniasih, NH Aprilita, R Roto and M Mudasir. Modification of coal fly ash for high-capacity adsorption of methylene blue. *Case Studies in Chemical and Environmental Engineering* 2025; **11**, 101101.

[42] SK Khandani, M Mehrabani, F Sharififar, A Pardakhty, M Pournamdari and M Pakravanan. Development and validation of an RP-HPLC method for determination of solasodine, a steroidal alkaloid. *Journal of Young Pharmacists* 2018; **11(1)**, 21-25.

[43] H Budi, AF Arsyada, H Saptono, K Soerja and K Azlan. Synthesis and characterization of chitosan-alginate hydrogel adsorbent for paracetamol removal from wastewater. *Trends in Sciences* 2025; **22(12)**, 10767.

[44] J Wang and X Guo. Adsorption isotherm models: Classification, physical meaning, application and solving method. *Chemosphere* 2020; **258**, 127279.

[45] SJ Santosa, ES Kunarti, NH Aprilita, B Wulandari and DN Bawani. Sorption mechanism and performance of peat soil humin for Methylene blue and p-Nitrophenol. *Indonesian Journal of Chemistry* 2019; **19(1)**, 198-210.